Materials Advances

ROYAL SOCIETY OF CHEMISTRY

PAPER

View Article Online
View Journal | View Issue

Cite this: *Mater. Adv.*, 2024, 5, 1597

An electrochemical immunosensor based on a nanostructured lanthanum oxide-substituted reduced graphene oxide interface for ultralow ciprofloxacin detection in milk samples†

Navneet Chaudhary,‡[ab] Amit K. Yadav, ‡[a] Damini Verma,[a] Jai Gopal Sharma[b] and Pratima R. Solanki *[a]

In the present work, we have reported a nanostructured lanthanum oxide nanoparticle-decorated reduced graphene oxide nanocomposite (nLa_2O_3 NPs@rGO)-based biosensing platform for efficient and label-free determination of ciprofloxacin (CPX) antibiotic. A facile hydrothermal method was utilized for the synthesis of the nLa_2O_3 NPs@rGO composite, followed by functionalization with 3-aminopropyltriethoxysilane (APTES) and attachment on an indium tin oxide (ITO)-coated substrate electrophoretically. The CPX monoclonal antibodies (anti-CPX) and bovine serum albumin (BSA) were immobilized using a drop-casting approach. The morphological, structural, and electrochemical characterization of nLa_2O_3 NPs@rGO and other developed immunoelectrodes was done through contact angle, X-ray diffraction (XRD), Fourier transform infrared (FT-IR), Raman spectroscopy, scanning electron microscopy (SEM), transmission electron microscopy (TEM), cyclic voltammetry (CV), differential pulse voltammetry (DPV), and electrochemical impedance spectroscopy (EIS). Here, rGO's large surface area assists in enhancing the nLa_2O_3 NPs dispersibility, which provides synergistic effects to the nLa_2O_3 NPs@rGO nanocomposite leading to electron transfer process acceleration. Hence, the developed immunoelectrode (BSA/anti-CPX/APTES/nLa_2O_3 NPs@rGO/ITO) effectively determines CPX having a broad linear detection range from 10^{-6} to 600 μg mL^{-1} with a lower detection limit of 0.055 μg mL^{-1} and good durability of 25 days. Furthermore, the immunosensor showed good selectivity towards CPX and was used in real samples of processed milk. Thus, the nLa_2O_3 NPs@rGO composite could emerge as a potential material for the determination of other antibiotics also.

Received 16th August 2023,
Accepted 18th November 2023

DOI: 10.1039/d3ma00556a

rsc.li/materials-advances

1. Introduction

Ciprofloxacin (CPX) is a 2nd generation fluoroquinolone that is utilized as an antibiotic against both Gram-negative and Gram-positive aerobic pathogens and is broadly applied to livestock and humans.[1–5] CPX has been discovered in surface water that are strongly affected by domestic wastewater and agricultural runoff effluents because the medicine is not fully metabolized.[6] Additional investigations have found CPX in cow's milk at concentrations greater than 0.1–100 ng mL^{-1}. Due to potential antibiotic-resistant bacteria growth, the existence of CPX as well as other antibiotics in the environment is a major concern.[7,8] As a result, active research is being carried out on the development of selective and sensitive sensors to determine the presence of antibiotics in the environment (such as milk, surface water, wastewater, *etc.*).

Many analytical techniques are being employed to determine CPX in different matrices, which include electrochemical,[9,10] immunoassay,[11] spectrofluorimetric,[12] capillary electrophoresis,[13] chemiluminescence,[14] spectrophotometry,[15,16] high-performance liquid chromatography[17] and liquid chromatography–mass spectroscopy[18] techniques. However, these analysis methods require expensive instrumentation, complex sample pre-treatment, and preparation, which cannot meet large-scale actual testing.[19,20] Moreover, some of them require the separation of the analytes before detecting them, which makes them expensive and not simple detection methods. For overcoming these disadvantages, we need a more cost-effective, simple, authentic, and rapid approach to CPX determination. In this regard, the electrochemical techniques (impedance spectroscopy,

[a] *Nano-Bio Laboratory, Special Centre for Nanoscience, Jawaharlal Nehru University, New Delhi-110067, India. E-mail: pratimarsolanki@gmail.com, partima@mail.jnu.ac.in; Tel: +91-011-26704740, +91-011-26704699*
[b] *Department of Biotechnology, Delhi Technological University, New Delhi-110042, India*

† Electronic supplementary information (ESI) available. See DOI: https://doi.org/10.1039/d3ma00556a

‡ These authors contributed equally to this work.

voltammetry) for the antibiotic's detection have prompted high research curiosity due to their rise in signal power to noise power ratio, simplicity, excellent sensitivity, low energy requirement, quick output time, ease of use, short time requirement, and low cost.[21–23]

The immobilization matrix's role in the fabrication of nano-immunosensing platforms is inevitable. Different metal oxides, for example zinc oxide (ZnO), titanium dioxide (TiO_2), magnesium oxide (MgO), iron oxide (Fe_3O_4), *etc.* have occupied a profound position as an efficient matrix support.[24,25] Among the metal oxides, nanostructured lanthanum oxide nanoparticles (nLa_2O_3 NPs) have gained more scientific curiosity among the research community, as it has a high surface area to volume ratio, excellent electrochemical properties, biocompatibility, chemical inertness, and high adsorption ability;[26–28] thus, could be efficiently employed for high biomolecule loading with the desired alignment. Moreover, nLa_2O_3 NPs also allow covalent bonding between the hydroxyl of ITO and silane groups of organosilanes like 3-aminopropyltriethoxysilane (APTES). Though many studies have described nLa_2O_3 NPs to form huge clusters owing to aggregation, functionalization of different metal oxides could deliver high surface area and high sensitivity for homogeneous dispersion of metal oxides as well analyte detection.[29,30]

Two-dimensional materials have gained consideration as promising candidates that could increase the surface area for metal oxide dispersion. Several studies in the past have shown that graphene and its derivatives, such as reduced graphene oxide (rGO), graphene oxide, *etc.*, have been used as sensing materials.[31] Among the derivatives, rGO containing different oxygen functional groups has displayed immense potential in the fabrication of nano-immunosensing platforms owing to its distinct properties, like the ability to facilitate electron transfer directly from biomolecules, high catalytic activity, good mechanical flexibility, remarkable conductivity, and excellent heterogeneous electron transfer.[32–34] The high surface area to volume ratio of rGO may help in the dispersion of metal oxides, thus preventing NPs agglomeration. The attachment of a metal oxide on the surface of the rGO sheet will be helpful in decreasing the steric hindrance occurring between the biomolecules.[35] In addition, the electrochemical performance is also reported to increase the large surface area and conductivity support for metal oxides.[36] An rGO sheet decorated with a nLa_2O_3 NPs-based biosensor has been effectively used for immobilization of enzymes and chlorpyrifos pesticide detection. Gupta and co-workers displayed electrochemical characteristics improvement and zirconium dioxide (ZrO_2) NPs low agglomeration by using a zirconium dioxide–reduced graphene oxide (ZrO_2–rGO) composite for ochratoxin determination.[37] Also, in another research study, homogenized zirconia-supported rGO has been employed as an efficient immobilization substrate for oral cancer detection.[38] In addition, 2D materials are being consistently used for point-of-care (POC) device development ascribed to their outstanding mechanical strength, favourable flexibility, tailor-made chemical and physical properties, *etc.* In several reports, these 2D material-based biosensors have been employed for the determination of various environmental and metabolic imperfection risk factors, comprising toxins and pathogens.[39,40] With these contemplations in mind, a nLa_2O_3 NPs@rGO composite appears to be a highly effective immobilization substrate for nano-immunosensing platform development, in which both the components synergistically pay off each other's limitations.

Most research on sensor development is focused on CPX detection in tablets, water, urine, and human serum, but the application of sensors to determine CPX in milk matrices has not been performed. Therefore, in this work, we fabricated a fast, selective, and sensitive, method for the detection of CPX in milk by indium tin oxide (ITO) electrode modification with a conductive nLa_2O_3 NPs@rGO film. Various modified electrodes were fabricated and set for testing to obtain selectivity and sensitivity toward CPX determination. The experimental results for CPX determination were obtained using electrochemical techniques [cyclic voltammetry (CV) and differential pulse voltammetry (DPV)] for different modified electrodes. The fabricated immunoelectrodes were characterized by X-ray diffraction (XRD), Raman, Fourier transform infrared spectroscopy (FT-IR), energy-dispersive X-ray (EDX), elemental mapping, scanning electron microscopy (SEM), transmission electron microscopy (TEM), contact angle measurement, DPV, and CV with common redox couples. The optimized immunosensor was utilized to detect CPX in processed milk and other interfering agents. The fabricated immunosensor has displayed remarkable biosensing parameters having linear ranges of 10^{-6} to 6600 μg mL^{-1} with a sensitivity of 6.52 μA mL μg^{-1} cm^{-2} with a regression coefficient (R^2) of 0.992 and LOD and LOQ of 0.055 μg mL^{-1} and 0.18 μg mL^{-1}, respectively. To the best of our knowledge, this is the first report on antibiotic (CPX) detection using the nLa_2O_3 NPs@rGO composite.

2. Experimental section

2.1. Materials and methods

Potassium hydroxide (KOH), acetone, hydrogen peroxide (H_2O_2), ethanol, and sodium hydroxide (NaOH) (98%) were purchased from fisher scientific, India. 1-(3-(Dimethylamino)-propyl)-3-ethylcarbodiimide hydrochloride (EDC), (3-aminopropyl)trimethoxysilane (APTES), acetonitrile (ACN), bovine serum albumin (BSA), and lanthanum nitrate tetrahydrate (99.99%) ($LaNO_3{\cdot}4H_2O$) were bought from Sigma Aldrich. Ciprofloxacin (CPX), uric acid, potassium ferricyanide ($K_3[Fe(CN)_6]$), potassium ferrocyanide ($K_4[Fe(CN)_6]{\cdot}3H_2O$), sodium monophosphate anhydrous [NaH_2PO_4], sodium diphosphate dihydrate [$Na_2HPO_4{\cdot}2H_2O$], sodium hydroxide (NaOH), and urea were procured from SRL Limited. *N*-Hydroxysulfosuccinimide (NHS)[$C_4H_5NO_3$] was purchased from Spectro Chem. The indium tin oxide (ITO) coated glass platform was obtained from Balzers, UK with 90% transmittance and 25 Ω sq^{-1} sheet resistance. For preparing the fresh phosphate buffer solution (PBS), NaH_2PO_4 as well as $Na_2HPO_4{\cdot}2H_2O$ were employed for making 0.2 M in distilled water (DI) having pH 7.0 and further kept in the refrigerator for the next

experiments. The specific ciprofloxacin (anti-CPX) monoclonal antibodies were bought from My BioSource, USA. All the reagents employed for the experiment were of analytical grade and utilized as such.

2.2. Instrumentation

An X-ray diffractometer (XRD) [Rigaku Miniflex 600 diffractometer (Japan), Cu-K radiation with monochromatic X-ray beam at λ = 1.54] was utilized for investigating the phase and crystal structure of the nLa_2O_3 NPs and nLa_2O_3 NPs@rGO-based nanocomposite. The data were recorded at room temperature (RT) with a 5° step size in the range of two theta from 10° to 80°. Fourier transform infrared spectroscopy (FT-IR, PerkinElmer, US) was employed for immobilizing the modified nLa_2O_3 NPs@rGO after it was functionalized with APTES utilizing anti-CPX as well as BSA-modified electrodes. High-resolution transmission electron microscopy (HR-TEM, JEM-2200 FS, Jeol, Japan) was utilized to analyze its structural and morphology aspects. For preparing the TEM sample, dispersion of the nLa_2O_3 NPs@rGO composite was done in ethanol followed by sonication for 5 h before it was drop-casted on a copper (Cu) grid covered with carbon (C) and dried overnight. The Raman active peaks for nLa_2O_3 NPs and nLa_2O_3 NPs@rGO were investigated by employing Raman spectroscopy [EnSpectr R532 (US)]. Utilizing the contact angle (CA) on the SURFTENS universal instrument (OEG GmbH Germany), researchers examined the hydrophobic or hydrophilic variations in ITO, APTES/nLa_2O_3 NPs@rGO/ITO, anti-CPX/APTES/nLa_2O_3 NPs@rGO/ITO, and BSA/anti-CPX/APTES/nLa_2O_3 NPs@rGO/ITO immunoelectrode. The autolab potentiostat/galvanostat electrochemical analyzer (Eco Chemie, The Netherlands) was employed for recording all the electrochemistry measurements linked to a computer with the NOVA software (version 1.10), which includes CV, frequency response analysis (FRA), and DPV. A 3-electrode system was used for carrying out the whole electrochemistry analysis in PBS of pH 7.0 with 5 mM $[Fe(CN)_6]^{3-/4-}$ redox coupler having BSA/anti-CPX/APTES/nLa_2O_3 NPs@rGO/ITO, platinum and Ag/AgCl as a working, counter, and reference electrode, respectively.

2.3. Synthesis of graphene oxide (GO)

The GO preparation using the modified Hummers' method has been described in our previously published research articles.[41,42]

2.4. Synthesis and functionalization of the nLa_2O_3 NPs@rGO composite

The nLa_2O_3 NPs@rGO composite was prepared *in situ* through a hydrothermal procedure. A one-pot, lower temperature, facile protocol was followed for forming nLa_2O_3 NPs on a 2D graphene derivative, *i.e.*, reduced graphene oxide (rGO). For this, 150 mg graphene oxide (GO) was weighed in 50 mL DI and 3 h sonication was performed to obtain a homogenous solution and stacked GO sheet exfoliation. Next, the other solution was made by the addition of 0.7 g of $La(NO_3)\cdot 4H_2O$ in 15 mL DI. This solution was added to the GO solution and stirred at 300 rpm for 15 min until a mixture solution was obtained. Afterwards, a dropwise addition of HCl (8 M) was done to make the above solution's pH acidic. Finally, the mixture solution was transferred to a 100 mL autoclaved Teflon vessel and placed in a muffle furnace at 160 °C for 6 h. The resulting solution was then centrifuged for 20 min at 9000 rpm, and washed with DI several times. The greyish-yellow-colored residue was collected and dried in an oven overnight at 60 °C as well as stored at RT for further use.

For functionalizing the prepared nLa_2O_3 NPs@rGO composite, a homogeneous solution was formed by mixing nLa_2O_3 NPs@rGO (50 mg) in 1 mg mL^{-1} isopropanol and stirring it at 300 rpm at 60 °C. Thus, the addition of 200 μL of APTES was done slowly with succeeding 5 mL Milli-Q water addition followed by stirring the solution for the subsequent 48 h. Finally, the filtration of the achieved product *i.e.*, APTES/nLa_2O_3 NPs@rGO, was performed using Whatman filter paper, and drying the sample for 4 h at 70 °C and kept at a dry location for further utilization.

2.5. Fabrication of the BSA/anti-CPX/APTES/nLa_2O_3 NPs@rGO/ITO nano-immunosensing platform

The first step was to hydrolyze ITO-coated substrates made from glass employing a 5 : 1 : 1 solution of water, H_2O_2, and NH_4OH for 1 h at 80 °C. The APTES/nLa_2O NPs@rGO composite (4 mg mL^{-1}) was disseminated in ACN using ultrasonication and increased surface charge through magnesium nitrate ($Mg(NO_3)_2\cdot 6H_2O$) for electrophoretic deposition (EPD). The thin layer of APTES/nLa_2O_3 NPs@rGO was deposited onto a pre-hydrolyzed ITO surface for 120 s at a DC of 60 V using a traditional 2-electrode setup with Pt and ITO serving as the cathode and anode, respectively with a 1 cm distance between them. For the purpose of immobilizing anti-CPX antibodies, a 30 μL solution comprising NHS of 0.4 M, anti-CPX of 50 μg mL^{-1}, as well as EDC of 0.2 M are mixed in a 1 : 2 : 1 ratio and allowed to preincubate for 45 min before being applied to the surface of the APTES/nLa_2O_3 NPs@rGO/ITO electrode. In order to lessen CPX's non-specific attachment, 20 μL of bovine serum albumin (BSA) was used after washing with PBS. The developed BSA/anti-CPX/APTES/nLa_2O_3 NPs@rGO/ITO immunosensor was subsequently rinsed with PBS and kept at 4 °C until further usage.[43,44] In Scheme 1, the developing processes for the BSA/anti-CPX/APTES/nLa_2O_3 NPs@rGO/ITO immunosensor are schematically depicted.

2.6. Determination of CPX in a milk sample

Stock solutions of various concentrations of CPX that range from 10^{-6} μg mL^{-1} to 600 μg mL^{-1} were made in PBS (pH 7.0) to validate the constructed immunosensor. To do this, the modified BSA/anti-CPX/APTES/nLa_2O_3 NPs@rGO/ITO was subjected to the stock solution of CPX for 10 min. The whole set of electrochemical tests for the immunosensor was completed utilizing the DPV in PBS with redox species. Additionally, a control analysis was carried out without using CPX.

By spiking samples of milk, the designed immunosensor was put to the test employing real samples. For spiked real sample analysis, food samples like milk were collected from a local market near the JNU campus. The milk samples (100 mL) underwent a pre-treatment process, involving the addition

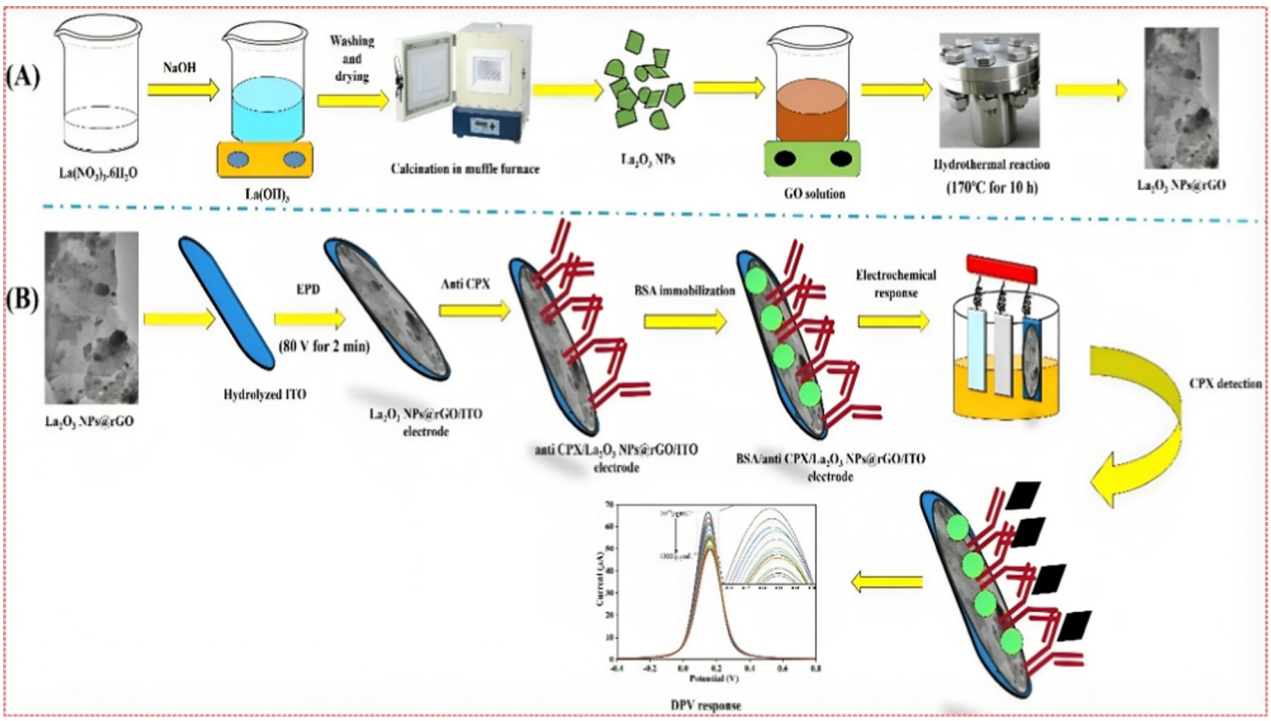

Scheme 1 (a) Schematic illustration of the chemically synthesized nLa_2O_3 NPs@rGO nanocomposite. (b) The developmental stages of the BSA/anti-CPX/ATPES/nLa_2O_3 NPs@rGO/ITO immunoelectrode for determination of CPX.

of 6 mL of 5 M methanol and 1 mL of 20 mM trichloroacetic acid. The mixture was thoroughly blended and then centrifuged at 10,000 rpm for 15 minutes at 25 °C. The resulting supernatant was slowly filtered to obtain the test sample. Subsequently, the sample was initially examined for the presence of CPX. If no signal change was detected, the samples were spiked. To create spiked milk samples, 20 μL of the treated milk was mixed with 3 mL of PBS containing a redox coupler at various CPX concentrations (ranging from 10^{-6} to 600 μg mL^{-1}). These spiked samples were utilized for sensing on the BSA/anti-CPX/APTES/nLa_2O_3 NPs@rGO/ITO immunosensor platform.[19] The sensing measurement for the immunosensor was conducted using these real spiked samples. The BSA/anti-CPX/APTES/APTES/nLa_2O_3NPs@rGO/ITO immunosensor was then applied to milk samples in order to find CPX antibiotics for 10 min. At RT (25 °C ± 2 °C), whole experiments were carried out thrice (n = 3).

3. Results and discussion

In this manuscript, the electrochemical nano-immunosensing based on nLa_2O_3 NPs@rGO nanocomposite approach was used for the first time to detect CPX using the DPV technique. The mechanism of electrochemical biosensing was established on the specific interaction among CPX and anti-CPX immobilized on the ITO electrode, as shown in Scheme 1, *i.e.*, the anti-CPX was made to attach on the APTES/nLa_2O_3 NPs@rGO/ITO surface covalently, which provides selectivity by capturing the CPX. The functionalization of antibodies and their subsequent immobilization on an amine-functionalized electrode during biosensor fabrication involves a well-established process mediated by EDC (1-ethyl-3-(3-dimethylaminopropyl)carbodiimide) and NHS (*N*-hydroxysuccinimide). This two-step mechanism begins with the activation of antibodies. First, EDC reacts with carboxyl groups on the antibody, forming a highly reactive *O*-acylisourea intermediate. To stabilize this intermediate and enhance its reactivity toward primary amines, NHS is introduced. This results in the formation of a stable NHS ester. This activated antibody is now ready for immobilization on the amine-functionalized electrode surface. The amine-functionalized electrode surface typically consists of molecules bearing primary amine groups. The key step in immobilization involves the formation of covalent amide bonds. The NHS ester on the activated antibody reacts with the primary amine groups on the electrode surface, creating a stable and covalent connection through amide bond formation. This covalent linkage firmly attaches the antibody to the electrode's surface, ensuring the specific and stable binding of the antibody to the amine-functionalized electrode. This EDC-NHS-mediated process results in a well-prepared amine-functionalized electrode with antibodies covalently anchored to its surface. These immobilized antibodies serve as the specific and selective capture elements for target analytes, forming the basis for the biosensor's function. Confirmation of successful immobilization is typically achieved through various analytical techniques, such as FT-IR spectroscopy, CV, DPV and EIS techniques.

3.1. Structural studies

XRD analysis. The synthesized nLa_2O_3 NPs@rGO composite's XRD spectrum is displayed in Fig. 1(a), which indicated its

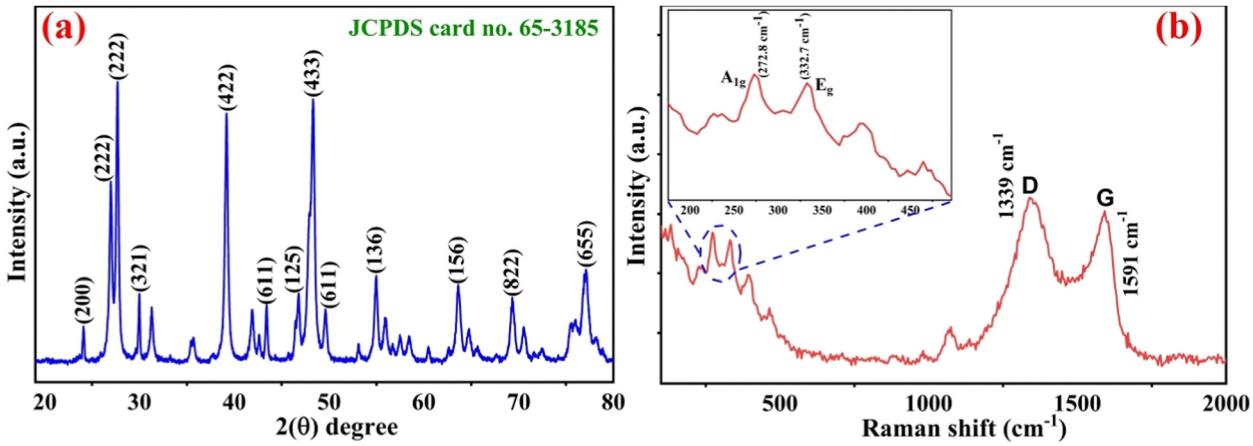

Fig. 1 (a) XRD spectrum; and (b) Raman curve of the nLa_2O_3 NPs@rGO composite.

phase purity and crystalline structure. At ambient temperature, a 2θ angle ranging from 10° to 80° was used for the XRD pattern investigation. The fact that the (002) plane is prominent at 23.6° shows that the reduction process results in the formation of crystalline rGO nanosheets.[45] The XRD structure exhibits peaks at 2θ = 24.1°, 26.9°, 27.7°, 30.0°, 39.1°, 43.3°, 46.6°, 48.3°, 49.1°, 54.9°, 63.6°, 69.4°, and 77.1°, that correspond to the nLa_2O_3 NPs alignments in accordance with the (200), (222), (222), (321), (422), (611), (125), (433), (611), (136), (156), (822) and (655) cubic planes, respectively. These findings demonstrate a strong correlation for the nLa_2O_3 NPs@rGO cubic phase with the JCPDS card no. 65-3185. The nLa_2O_3 NPs@rGO composite samples show excellent insertion of nLa_2O_3 NPs into rGO due to the existence of (002) planes along with nLa_2O_3 NP peaks. The remarkable crystallinity of nLa_2O_3 NPs@rGO is demonstrated by the well-defined, sharp, and strong peaks.[46,47] Therefore, nLa_2O_3 NPs@rGO's body-centered lattice with cubic phase formation is confirmed by its XRD characterization, and no other impurity peaks were found. Additionally, as demonstrated in Fig. S1 (ESI†) the XRD results show that the nLa_2O_3 NPs have a hexagonal structure. The Scherrer formula was used to calculate the crystallite size (D) of the nLa_2O_3 NPs@rGO NPs, and the D value was calculated as 30.9 nm corresponding to 2θ = 29.6 (grain) as provided below:

$$D = K\lambda/\beta \cos\theta \quad (1)$$

where K stands for the dimensionless shape factor (0.9), λ is the target's wavelength (Cu-Kα: 1.540 Å), θ is the Bragg's diffraction angle, and β is the full width at half maximum (FWHM) of the diffraction peak.

Raman analysis. To investigate the phonon vibrational patterns of the chemical bonds, particularly in crystalline samples, Raman spectroscopy is a valuable instrument. This technique is widely known for identifying secondary phases. This characterization method may identify a variety of flaws in complex layers and is highly sensitive to microcrystals. Therefore, Raman analysis was performed on our synthetic material to verify that rGO had successfully hybridized with nLa_2O_3 NPs. The nLa_2O_3 NPs@rGO composite's Raman active modes are depicted in Fig. 1(b). Two distinctive peaks in the rGO's Raman spectra can be seen at 1591 cm^{-1} (G band) and 1339 cm^{-1} (D band). In the pure nLa_2O_3 NP sample, two distinctive peaks have been seen. The La–O stretching vibration is attributed to the E_g band at 410 cm^{-1}, while the La–O bending vibration is ascribed to the A_{1g} band at 208 cm^{-1}.[48] The degree of defects or disorder in graphene-based derivatives is assessed using the intensities of the D band (ID) to G band (IG) *i.e.*, by the ID/IG ratio. The ID/IG ratio similarly falls to 0.92 from 1.23 in this case. These were caused by the oxygen-rich rGO being reduced during the nLa_2O_3 NPs formation. Additionally, this conclusion is supported by the XRD study. Fig. S2 (ESI†) displays the pure nLa_2O_3 NPs' Raman spectra.

3.2. Morphological studies

Both TEM and SEM techniques were used to examine the morphological characteristics of the developed electrode samples.

Transmission electron microscopy. TEM was employed to examine the size, shape, and morphology of the as-prepared nLa_2O_3 NPs@rGO composite [Fig. 2(a)–(d)]. In both the figures, the nLa_2O_3 NPs are highly agglomerated and diffused into the thin layer of rGO, thereby depicting that nLa_2O_3 NPs can be seen adhering to the wrinkly rGO surface. This is the reason that NPs are not clearly visible separately. However, the sheet-like structure of the rGO is depicted in Fig. 2(a) and (b), with wrinkled and folded structures suggesting a minimal number of layers. Additionally, the selected area electron diffraction (SAED) ring trends [Fig. 2(c)], which show the nLa_2O_3 NPs diffraction rings in the nLa_2O_3 NPs@rGO composite, are in accordance with the nLa_2O_3 NP planes, representing an extremely crystalline nature of nLa_2O_3 NPs. As is widely recognized, single-crystal solids exhibit a patchy diffraction pattern in SAED while polycrystalline substances exhibit a ring distribution.[49] As a result, the resulting rings are clearly defined, indicating strong crystallinity and a polycrystalline character. Additionally, it is discovered that these results and the XRD data are in good agreement. As shown in Fig. 2(d), the HR-TEM picture of rGO and nLa_2O_3 NPs in the nLa_2O_3 NPs@rGO composite displays a

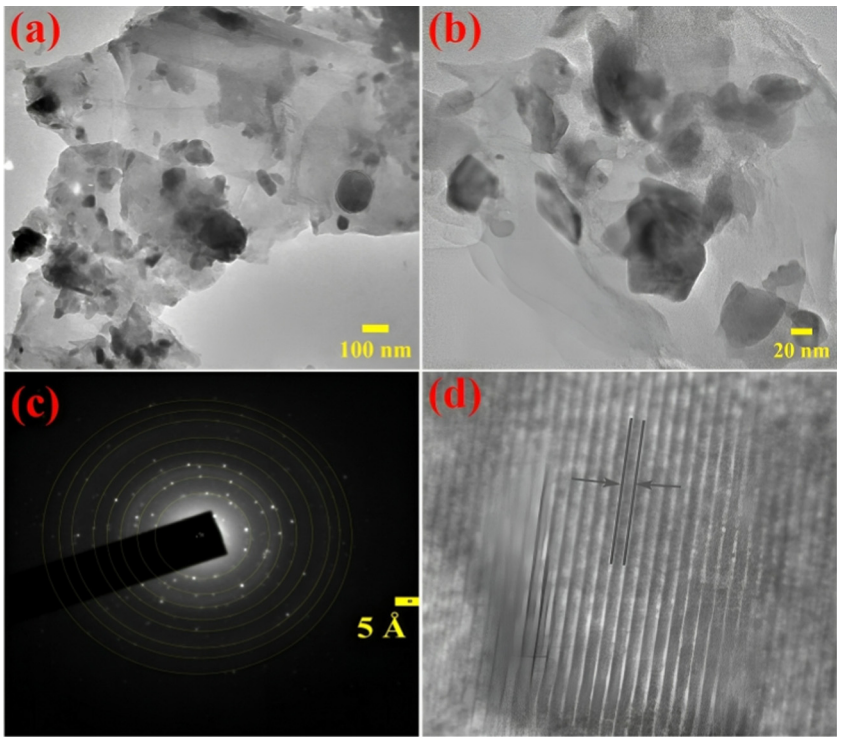

Fig. 2 (a) and (b) TEM pictures of the nLa_2O_3 NPs@rGO composite depicting the rGO sheet-like structure in high and low magnification; (c) SAED pattern; and (d) HR-TEM picture of the nLa_2O_3 NPs@rGO nanocomposite depicting the (222) crystal plane of nLa_2O_3 NPs.

distinct 0.31 nm lattice fringe value that corresponds to the (222) plane, which happens to be the nLa_2O_3 NPs largest orientation plane, as well as 0.385 nm ascribed to the rGO (002) plane, which is supported by XRD findings.

Scanning electron microscopy. The scanning electron microscopy (SEM) characterization was completed and offered a useful method to visualize the nanomaterial surface. The top-facing SEM images of the nLa_2O_3 NPs@rGO composite are shown in Fig. 3(a). The nLa_2O_3 NPs were dispersed more evenly throughout the rGO sheets as can be seen from Fig. 3(a). The filaments' composition and structure were investigated using EDX. This technique is utilized for qualitative examination and investigates the energy and wavelength of the material's irritated X-rays, as well as the elemental detection. The EDX picture, which consists of C, O, and La components, displayed in Fig. 3(b), also clearly demonstrates the effective insertion of nLa_2O_3 NPs to the rGO surface. Each peak in this graph corresponds to an atom based on its energy. Large peaks reflect that an element's concentration in the sample is increased. The elemental compositions in % are 59.83 $\pm$ 1.23 wt% for La, 11.23 $\pm$ 0.35 wt% for C and 28.94 $\pm$ 0.79 wt% for O. The calculated composition is consistent with what has been determined theoretically.

The nLa_2O_3 NPs@rGO nanocomposite distribution characteristics as well as the specific and dominant elements, *i.e.*, C, O, and La, were further investigated using the elemental mapping method. The elemental mapping investigation for the nLa_2O_3 NPs@rGO composite, [Fig. 3(c)] revealed a flawless homogeneous distribution of the C, O, and La elements in the sample. The EDX findings showing the existence of C, O, and La elements in the sample were also supported by elemental mapping investigation. The existence of the C, O, and La elements in the corresponding active sample, depicted in Fig. 3(c), is confirmed by elemental map assessment, which displays each element in a sample's area.

3.3. Fourier transformed infrared spectroscopy (FT-IR) studies

The vibrational modes and functional groups present in the synthesized samples were proved by spectral investigation, which was carried out utilizing a PerkinElmer FT-IR spectrometer ranging from 4000–400 cm^{-1}. Fig. 4(a) shows the measured spectrum of the APTES/nLa_2O_3 NPs@rGO/ITO electrode. The absorption band at 1589 cm^{-1} in the FT-IR curve of rGO corresponds to the C=C stretching vibration and characteristics of sp^2 bonding. The C–OH and C=O vibration modes of stretching of the –COOH functional group were assigned to the bands at 1108 cm^{-1} and 1603 cm^{-1}, respectively. The La–O's stretching vibrations can be seen by peaks from 1108 to 852 cm^{-1}, whereas its twisting oscillations are indicated by the peaks from 649 to 556 cm^{-1}.[50] The prominent peaks discovered at 3703 cm^{-1}[138] further support the O–H stretching presence, which is compatible with the moisture absorbed on the surface of the sample. The FT-IR curve of the nLa_2O_3 NPs@rGO composite contained all of the characteristic functional groups associated with rGO and La_2O_3 NPs. Additionally, peaks at 1636 and 1949 cm^{-1} were seen that correspond to the amide II peak and –CO stretching, respectively, produced between the anti-CPX's –COOH group and the APTES/nLa_2O_3 NPs@rGO/ITO amine group, suggesting the antibodies' adherence to the functionalized nanocomposite[51]

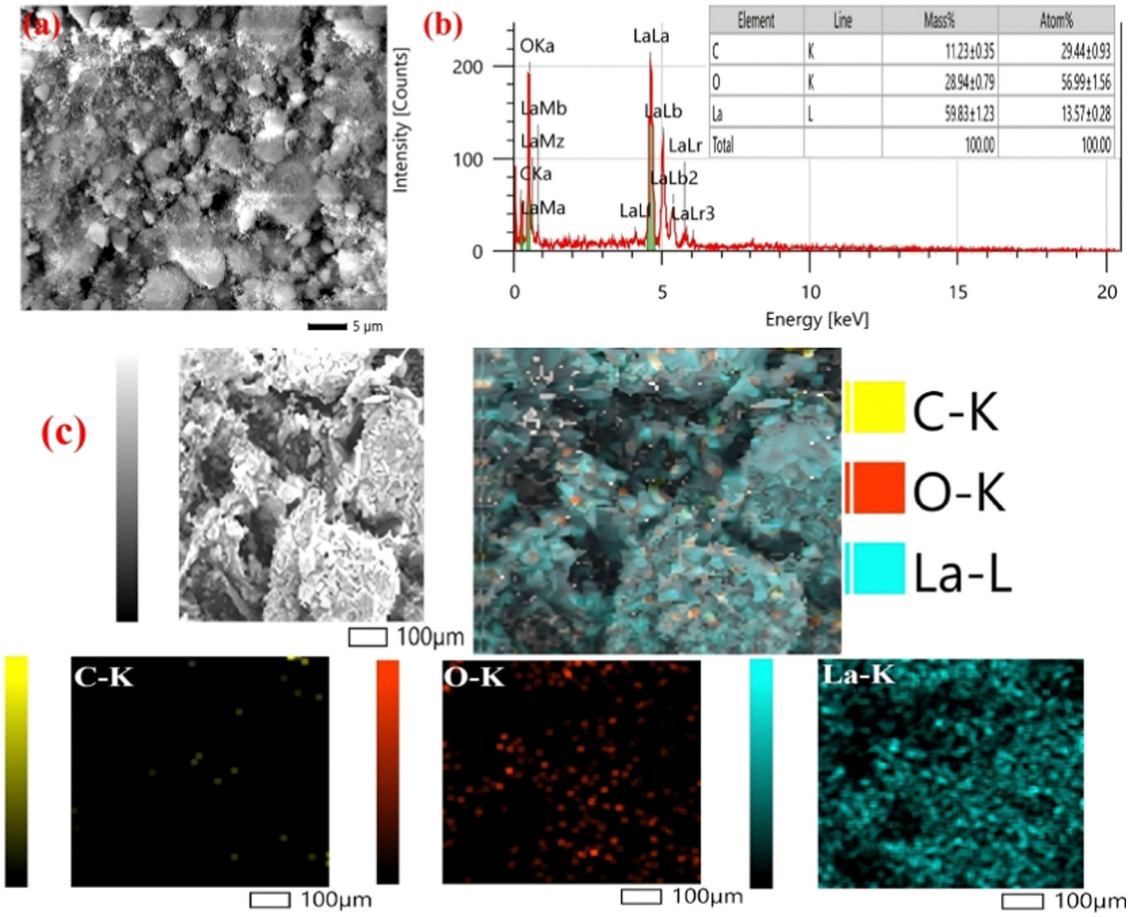

Fig. 3 (a) SEM pictures; (b) EDX spectrum; and (c) elemental mapping of the nLa_2O_3 NPs@rGO composite.

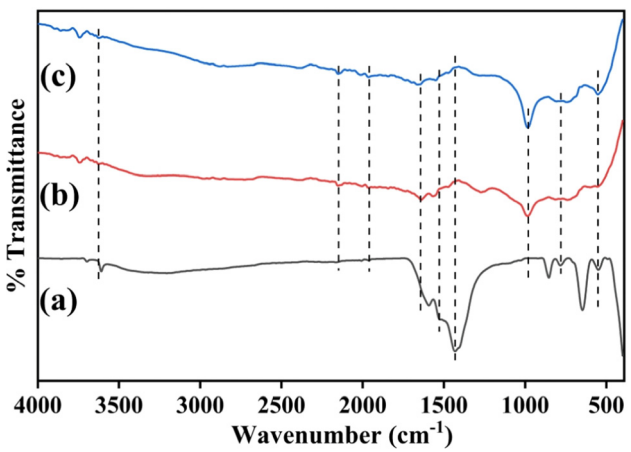

Fig. 4 FT-IR spectra of (a) APTES/nLa_2O_3 NPs@rGO/ITO electrode; (b) anti-CPX/APTES/nLa_2O_3 NPs@rGO/ITO electrode; and (c) BSA/anti-CPX/APTES/nLa_2O_3 NPs@rGO/ITO immunoelectrodes.

[Fig. 4(b)]. Furthermore, the peak at 1428 and 1487 cm^{-1} got vanished, and the peak intensities of 1636 and 1949 cm^{-1} decreased, as illustrated in Fig. 4(c), confirming the immunoelectrode's blockage by BSA particles.

3.4. Contact angle studies

For estimating the contact angle, the sessile drop method is employed after modifying every stage of fabrication to assess the hydrophobic or hydrophilic activity of the developed electrodes [Fig. S3(a)–(d), ESI†]. The hydrophobic character of the unmodified hydrolyzed ITO electrode has been demonstrated by the CA value (75.7°), which is illustrated in Fig. S3(a) (ESI†). The CA value grew to 119.5° [Fig. S3(b), ESI†] after the nLa_2O_3 NPs@rGO nanocomposite's EPD on the ITO electrode, suggesting the extremely hydrophobic property of the APTES/nLa_2O_3 NPs@rGO/ITO electrode providing a suitable condition for anti-CPX immobilization. Furthermore, the value of CA was reduced to be 21.0° [Fig. S3(d), ESI†] and 40.6° [Fig. S3(c), ESI†] after BSA and anti-CPX immobilization of molecules, respectively, on the surface of the APTES/nLa_2O_3 NPs@rGO/ITO electrode, demonstrating a rise in hydrophilic behavior of the BSA/anti-CPX/APTES/nLa_2O_3 NPs@rGO/ITO immunoelectrode and anti-CPX/APTES/nLa_2O_3 NPs@rGO/ITO electrode due to the covalent relation between the APTES/nLa_2O_3 NPs@rGO electrode and anti-CPX.[36] This hydrophilicity helps to boost sensitivity and improve antigen adhesion in PBS.[43,52]

3.5. Electrochemical characterization studies

pH and electrode study. At first, optimization of the best experimental parameters for electrochemical characterization

was done by employing a variety of PBS solutions with different pH levels through pH studies. DPV responses were measured in potential ranges that extend from −0.4 V to +0.8 V to explore the impact of pH (6.0–9.0) on the electrochemical characteristics of the constructed nano-biosensor (BSA/anti-CPX/APTES/nLa_2O_3 NPs@rGO/ITO). As can be seen from Fig. 5(a), the highest peak current is seen at pH 7.0, which could be due to the antibodies that are present in their original state at neutral pH and have the most activity therein, while they tend to get destroyed in the basic or acidic environment.[53] Thus, a PBS buffer having pH 7.0 was employed to conduct further electrochemical investigations.

Additionally, in the presence of PBS pH 7.0 comprising $[Fe(CN)_6]^{3-/4-}$ as a redox coupler, the electrochemical features of the developed electrodes have been investigated using DPV and CV. To examine the peak current variations at various stages of electrode alteration, the electrochemical behaviors of the BSA/anti-CPX/APTES/nLa_2O_3 NPs@rGO/ITO (curve iv), anti-CPX/APTES/nLa_2O_3 NPs@rGO/ITO (curve iii), APTES/nLa_2O_3 NPs@rGO/ITO (curve ii), and ITO (curve i) electrodes were monitored *via* CV having the potential window ranging from −0.8 V to +0.8 V and the outcomes achieved are displayed in Fig. 5(b). It was discovered that the APTES/nLa_2O_3 NPs@rGO/ITO electrode's peak current was improved (251.80 μA) compared to the ITO electrode (228.17 μA). The rapid transfer of electron kinetics from electrolyte to electrode and superior electrochemical characteristics, which contribute to increased current, have been rendered possible by the high electrical conductivity of rGO found in nLa_2O_3 NPs@rGO. Furthermore, the addition of incorporated nLa_2O_3 on the rGO sheets allows for the transfer of different ions across the interface of the electrodes *via* its permeable pathways, which enhances the peak current in a synergistic manner.[54] The peak current jumped to 291.16 μA once the antibody (anti-CPX) was immobilized, indicating a quick electron transport to the electrode's surface. This was possible because nLa_2O_3 NPs@rGO acted as a mediator at the surface of ITO and significantly shortened the distance over which electrons could tunnel from the anti-CPX to the electrode. Additionally, non-covalent interaction between the redox species and unbound anti-CPX –NH_2 terminal was the cause of the immunoelectrode's rapid diffusion of electrons.[55,56] This demonstrated that the antibodies were successfully immobilized. The peak current also dropped to 280.36 μA following the attachment of BSA on the anti-CPX/APTES/nLa_2O_3 NPs@rGO/ITO immunoelectrode. It could be due to the non-specific active regions on the surface of the immunoelectrode that have been blocked. In addition, DPV was also obtained for all the electrodes in the −0.6 V to +0.8 V potential window at a 50 mV s^{-1} scan rate, showing comparable results such as in CV [Fig. 5(c)]. These results demonstrate an

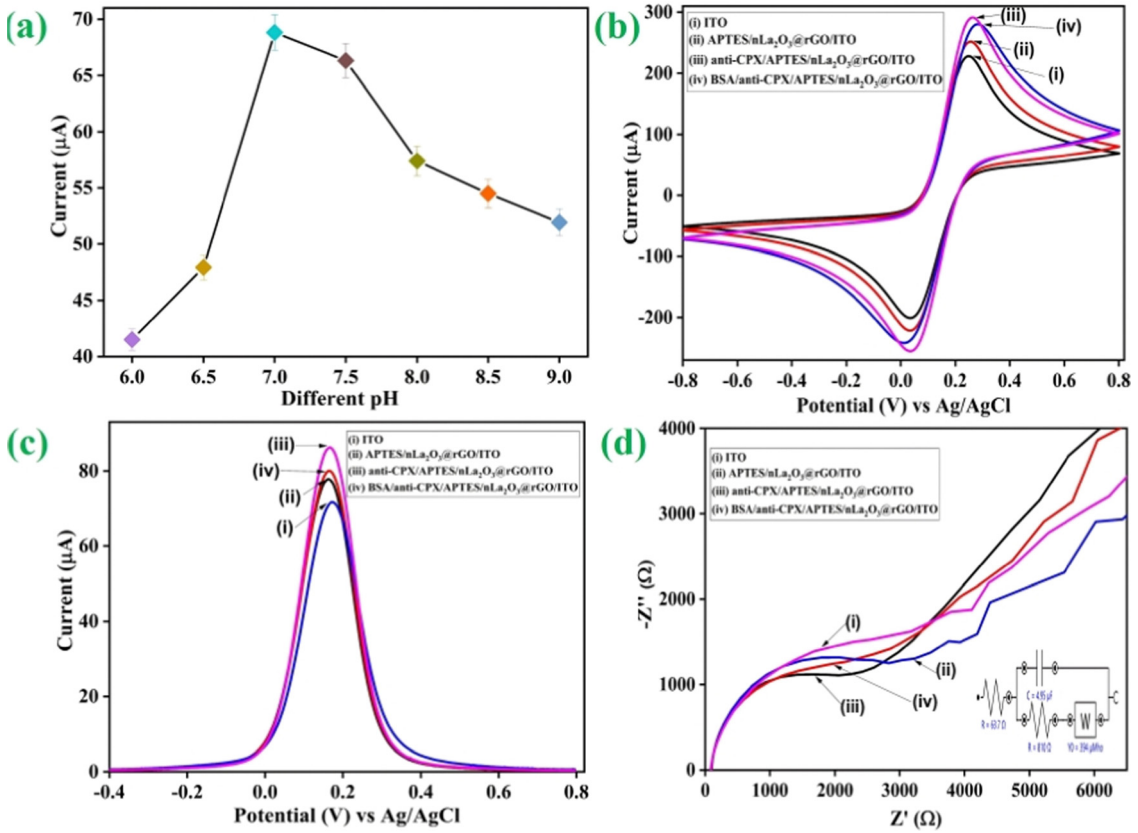

Fig. 5 (a) pH effect of BSA/anti-CPX/APTES/nLa_2O_3 NPs@rGO/ITO immunoelectrode; (b) CV; (c) DPV; and (d) EIS study of ITO (curve i), APTES/nLa_2O_3 NPs@rGO/ITO (curve ii), anti-CPX/APTES/nLa_2O_3 NPs@rGO/ITO (curve iii) and BSA/anti-CPX/APTES/nLa_2O_3 NPs@rGO/ITO (curve iv) electrodes [inset depicts the Nyquist circuit diagram].

effective and sequential fabrication process for an immunoelectrode, as shown by the contact angle, FT-IR, and SEM analyses.

As indicated by Fig. 5(d), further impedance spectra were recorded in the 100 Hz to 10 Hz frequency range [the inset displays the Nyquist circuit schematic diagram]. Various properties such as time constant (τ), heterogeneous electron transfer rate constant (K_{ct}), and charge transfer resistance (R_{ct}) have been determined for BSA/anti-CPX/APTES/nLa_2O_3 NPs@rGO/ITO (curve iv), anti-CPX/APTES/nLa_2O_3 NPs@rGO/ITO (curve iii) APTES/nLa_2O_3 NPs@rGO/ITO (curve ii), and ITO (curve i) electrodes as described in Table S1 (detailed information can be found in the ESI†).

Interfacial kinetics studies. By examining changes in peak current *versus* varying scan rates from 10 to 100 mV s^{-1}, the interfacial kinetics of the BSA/anti-CPX/APTES/nLa_2O_3 NPs@rGO/ITO immunoelectrode and APTES/nLa_2O_3 NPs@rGO/ITO electrodes were studied *via* CV in the −0.8 V to +0.8 V potential range. Both the anodic (I_{pa}) and cathodic (I_{pc}) peak current magnitudes exhibit a linearly rising pattern against the square root of scan rate, as illustrated in [Fig. 6A(i) and B(i)], indicating that the electrochemical system is diffusion regulated[9,57] and implies eqn (2)–(5).

$$I_{pa(APTES/nLa_2O_3\ NPs@rGO/ITO)} = -[17.63\ \mu A\ (s\ mV^{-1}) \times (\text{scan rate } [mV\ s^{-1}])^{1/2}] - 63.92\ \mu A,\ R^2 = 0.978 \quad (2)$$

$$I_{pc(APTES/nLa_2O_3\ NPs@rGO/ITO)} = [21.93\ \mu A\ (s\ mV^{-1}) \times (\text{scan rate } [mV\ s^{-1}])^{1/2}] + 65.94\ \mu A,\ R^2 = 0.989 \quad (3)$$

$$I_{pa(BSA/anti\text{-}CPX/APTES/nLa_2O_3\ NPs@rGO/ITO)} = -[21.42\ \mu A\ (s\ mV^{-1}) \times (\text{scan rate } [mV\ s^{-1}])^{1/2}] - 71.63\ \mu A,\ R^2 = 0.986 \quad (4)$$

$$I_{pc(BSA/anti\text{-}CPX/APTES/nLa_2O_3\ NPs@rGO/ITO)} = [26.87\ \mu A\ (s\ mV^{-1}) \times (\text{scan rate } [mV\ s^{-1}])^{1/2}] + 67.23\ \mu A,\ R^2 = 0.992 \quad (5)$$

On increasing the sweep rate, the I_{pc} and I_{pa} values change to greater both negative and positive potentials, respectively. The E_{pa} and E_{pc} represent anodic and cathodic peak potentials, respectively, and their magnitude difference ($\Delta E_p = E_{pa} - E_{pc}$) exhibits a linear fluctuation with scan rate squared. The findings, which are reflected in eqn (6) and (7), are displayed in [Fig. 6A(ii) and B(ii)] and demonstrate the easy charge transfer kinetics between the electrode interface and medium. These outcomes demonstrated the suitability of the fabricated electrodes for electrochemical biosensing purposes.

$$\Delta E_p(V)_{(APTES/nLa_2O_3\ NPs@rG/ITO)} = [0.024\ V\ (s\ mV^{-1}) \times (\text{scan rate } [mV\ s^{-1}])^{1/2}] + 0.085\ V,\ R^2 = 0.993 \quad (6)$$

$$\Delta E_p(V)_{(BSA/anti\text{-}CPX/APTES/nLa_2O_3\ NPs@rGO/ITO)} = [0.023\ V\ (s\ mV^{-1}) \times (\text{scan rate } [mV\ s^{-1}])^{1/2}] + 0.093\ V,\ R^2 = 0.994 \quad (7)$$

An essential factor that can be used to predict the fabrication electrode's ability for biosensing is the diffusion co-efficient (D). The D value at the interface between the BSA/anti-CPX/APTES/nLa_2O_3 NPs@rGO/ITO immunoelectrode and redox couple $[Fe(CN)_6]^{3-/4-}$ is calculated using the Randles–Sevcik equation.

$$I_p = (2.69 \times 10^5) C n^{3/2} D^{1/2} \upsilon^{1/2} A \quad (8)$$

where A depicts the working electrode's surface area, *i.e.*, 0.25 cm^2, I_p depicts the electrode's peak current, C stands for the redox species' concentration, D depicts the diffusion coefficient ($cm^2\ s^1$), and υ depicts 0.05 V s^{-1} scan rate. The estimated D value is 9.71×10^{-4} $cm^2\ s^{-1}$.

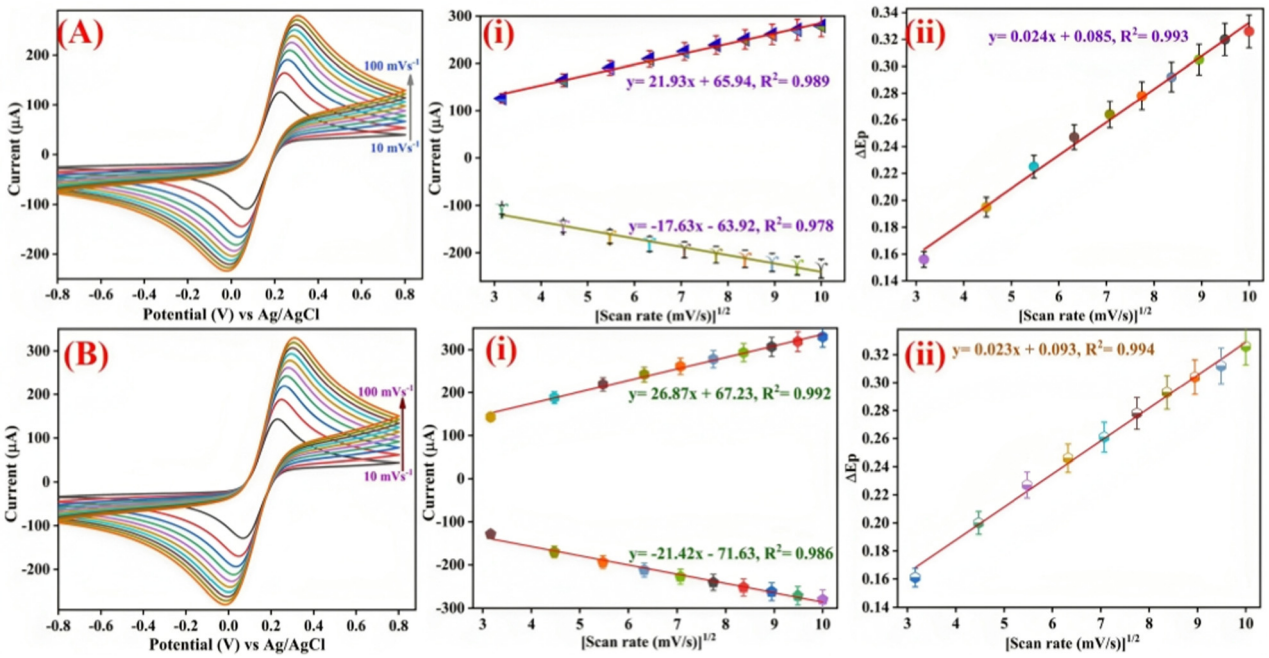

Fig. 6 CV of the (A) APTES/nLa_2O_3 NPs@rGO/ITO electrode; and (B) BSA/anti-CPX/APTES/nLa_2O_3 NPs@rGO/ITO immunoelectrode at various scan rates ranging from 10 to 100 mV s^{-1}, (A(i)) and (B(i)) calibration curve showing cathodic and anodic current *versus* square root of scan rate, (A(ii)) and (B(ii)) potential difference ($\Delta E_p = E_{pa} - E_{pc}$) *versus* square root of the scan rate.

Additionally, the following has been calculated using the Brown–Anson equation [eqn (9)] to represent the anti-CPX surface concentration on the immunoelectrode electrode surface:

$$I_p = \frac{n^2F^2\gamma^*A\upsilon}{4RT} \quad (9)$$

where T depicts 298 K temperature, υ stands for scan rate (50 mV s^{-1}), R depicts the gas constant, *i.e.*, 8.314 J mol^{-1} K^{-1}, n depicts a number of electron transfers (*i.e.*, 1), F is the Faraday constant (96 584 C mol^{-1}), A is the electrode surface area (0.25 cm^2), v is the scan rate (50 mV s^{-1}), I_p is the immunoelectrode current and γ stands for absorbed electro-active species' surface concentration (mol cm^{-2}). The BSA/anti-CPX/APTES/nLa_2O_3 NPs@rGO/ITO immunoelectrode surface concentration of anti-CPX was determined as 3.23 × 10^{-8} mol cm^2, which suggests that the immunoelectrode might have effective biosensing attributes.

Electrochemical response studies. An incubation analysis was conducted before the electrochemical response experiments for the developed immunosensor to determine an approximate time frame for the attachment of antibodies and antigens. To investigate the fluctuation in current values when CPX interacts with the proposed BSA/anti-CPX/APTES/nLa_2O_3 NPs@rGO/ITO immunoelectrode for various time periods, *i.e.*, from 0 to 16 min, a DPV study was carried out. An incubation-period study with a decreasing peak current in relation to time is shown in Fig. 7(a). The peak current has been seen to fall to 14 min, after which the peak current reaches saturation. According to the data, CPX antibiotics must bind to the BSA/anti-CPX/APTES/nLa_2O_3 NPs@rGO/ITO immunoelectrode for 14 min. Therefore, 14 min are provided for the investigation of the various CPX levels of antibiotics to conduct subsequent electrochemical response experiments.

We evaluated the CPX at different concentrations using DPV approaches to assess the analytical characteristic of the nLa_2O_3 NPs@rGO-derived immunosensor, as illustrated in Fig. 7(b). The determination of CPX using a biosensing platform has made extensive use of the versatile and effective electrochemical DPV approach. In this method, a 3-electrode system was used with Ag/AgCl, the proposed immunosensor, and platinum electrodes functioning as a reference, working, and counter electrode, respectively. The DPV spectra of the constructed BSA/anti-CPX/APTES/nLa_2O_3 NPs@rGO/ITO immunoelectrode were obtained under the best experimental circumstances following incubation with various CPX antibiotic concentrations ranging from 10^{-6} to 1000 μg mL^{-1} at 50 mV s^{-1} scan rate in the 0.4 to +0.8 V potential window. After 15 min of engagement with different CPX

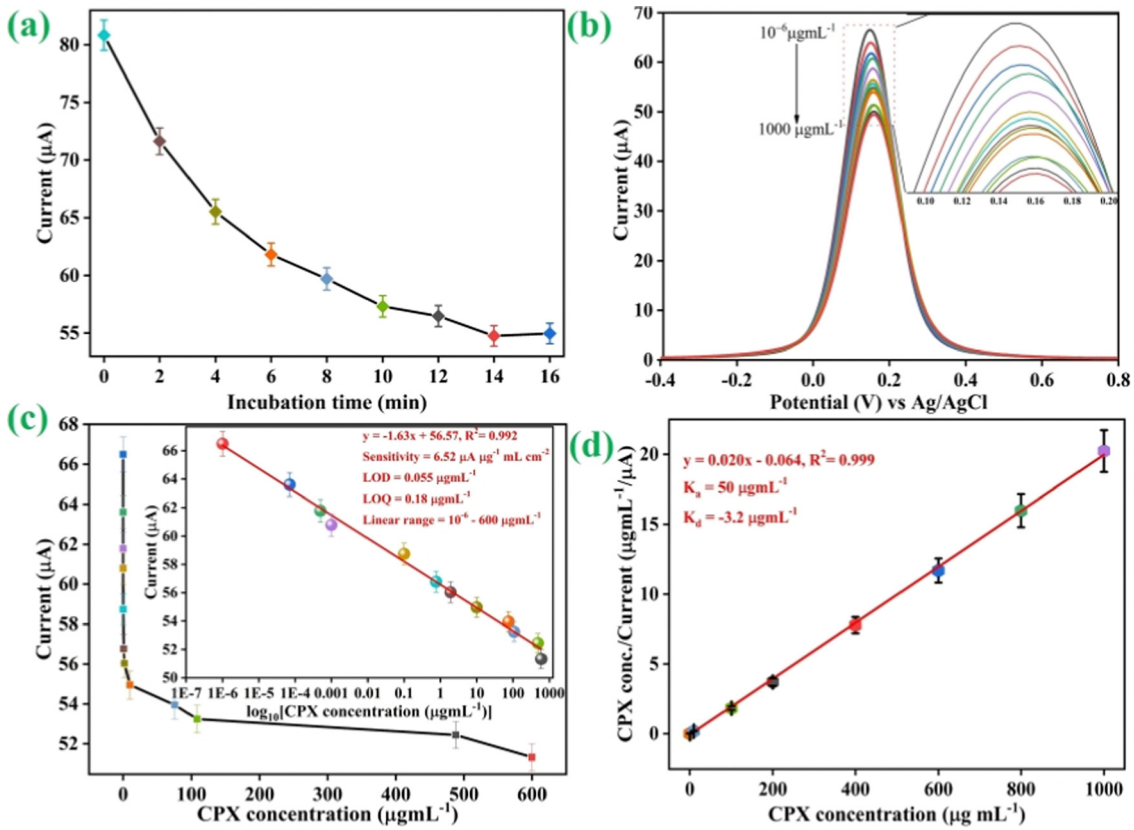

Fig. 7 (a) BSA/anti-CPX/APTES/nLa_2O_3 NPs@rGO/ITO immunoelectrode's incubation analysis for attachment of CPX to the immunoelectrode surface, (b) electrochemical response studies of BSA/anti-CPX/APTES/nLa_2O_3NPs@rGO/ITO immunoelectrode as a function of concentration of CPX, *i.e.*, 10^{-6}–1000 μg mL^{-1} using DPV [inset displayed the zoomed magnification]; (c) linear plot of peak current *versus* concentration of CPX (μg mL^{-1}); the inset shows the calibration plot between peak current *versus* $\log_{10}$ concentration of CPX (μg mL^{-1}); and (d) the BSA/anti-CPX/APTES/nLa_2O_3 NPs@rGO/ITO immunoelectrode's Hens–Wolf plot.

concentrations, immunoelectrodes are shown to have a DPV response as in Fig. 7(b). The peak current gradually dropped from 10^{-6} to 1000 μg mL^{-1} as the CPX concentration is raised because more immunological complexes between CPX and anti-CPX antibody are formed, preventing the electron transfer [Fig. 7(b)], and then became steady after adding 1000 μg mL^{-1}. The development of an electrically insulating immunocomplex, which prevents the transmission of electrons between electrolytic species $[Fe(CN)_6]^{3-/4-}$ and the immunoelectrode, is thought to be the cause of the drop in peak current noticed following the addition of CPX antibiotics.[58,59] This decline also demonstrated that the CPX antibiotics were successfully attached to the immunoelectrode surface following the reaction. In conclusion, the amount of immune complex formed on the immunoelectrode interface was the source of the drop in peak current. The enlarged area of the DPV plot is shown in the inset.

As observed in Fig. 7(c), the variation in the current (I) exhibited an excellent linear correlation with the CPX concentration ranging from 10^{-6} to 600 μg mL^{-1} under the optimal circumstances. The following equation, which has a 0.992 linear regression coefficient, is obtained from the calibration graph involving peak current as well as standard concentrations of CPX.

$$I_p = [-1.63\ (\mu A\ mL\ \mu g^{-1}) \times \text{conc. of CPX}\ (\mu g\ mL^{-1})] + 56.57\ \mu A,\ R^2 = 0.992 \quad (10)$$

This showed that the immunocomplex formed between the anti-CPX and CPX, particularly on the BSA/anti-CPX/APTES/nLa_2O_3NPs@rGO/ITO immunosensing platform, offered fewer electroactive areas for unstrained transfer of electrons at the electrode surface that resulted in thickness broadening of insulating layer development because of which the current dropped in proportion to the CPX concentration. The sensitivity value for the manufactured BSA/anti-CPX/APTES/nLa_2O_3 NPs@rGO/ITO immunosensor electrode was determined as 6.52 μA mL μg^{-1} cm^2 having 0.992 R^2 determined by the slope of the linear plot/surface area of the electrode, *i.e.*, 0.25 cm^{-2}. The limit of quantification (LOQ: $10\sigma/m$) and limit of detection (LOD: $3\sigma/m$) where m stands for the linear plot's sensitivity and σ depicts the intercept's standard deviation, were discovered to be 0.18 μg mL^{-1} and 0.055 μg mL^{-1}, respectively. The immunosensor also has a broad linear detection range between 10^{-6} and 600 μg mL^{-1}. The distinctive interaction between CPX and anti-CPX and the thin film generation of well-ordered nLa_2O_3 NPs@rGO composites may be the source of the immunosensor's high sensitivity. Having an efficient covalent connection with a widely recognized amide bond, APTES functionalized nLa_2O_3 NPs@rGO produced an ideal matrix for effective antibody attachment.

The improved BSA/anti-CPX/APTES/nLa_2O_3 NPs@rGO/ITO immunosensor outperformed other sensors in terms of wide detection range, LOD, and sensitivity, in comparison with earlier investigations (Table 1). This occurred as a result of the antibodies and the modified nanocomposite, which increased the number of reactive functional sites on the ITO surface electrode and boosted more efficient CPX binding. Additionally, the process was gentle and didn't damage the electrode surface, which assisted in recognizing responsive CPX. According to our review of the literature, this study provides the first account of the development of an electrochemical immunosensor for the detection of CPX using a nLa_2O_3 NPs@rGO composite in just 14 min.

In addition, the value of association constant (K_a) for the BSA/anti-CPX/APTES/nLa_2O_3 NPs@rGO/ITO immunoelectrode shown in Fig. 7(d) was determined from the Hens–Wolf graph, which consists of a plot relating CPX concentration with CPX conc./current and estimated to be 50 μg mL^{-1}. K_a depends on

Table 1 Comparative table depicting the BSA/anti-CPX/ATPES/nLa_2O_3 NPs@rGO/ITO biosensor' electrochemical parameters to earlier published data against CPX determination

Sensor/biosensor	Technique	Sensitivity (μA μg mL^{-1})	LOD (μg mL^{-1})	Linear range (μg mL^{-1})	Sample	Ref.
$MgFe_2O_4$-MWCNT/GCE	CV		0.01	0.1–1000	Tablet, plasma, and urine	60
PAR/EGR/GCE	DPV	—	0.01	0.04–10 and 10–120	Pharmaceutical preparation and biological media	61
P-β-CD-L-arg/CPE	DPV	—	0.05	0.05–100	Pharmaceutical formulations and human serum	62
DNA biosensor	DPV	—	9	40–80	—	63
NiONPs-GO-CTS: EPH/GCE	SWV	9.87	6.0×10^{-3}	0.040–0.97	Urine, serum	64
MWCNT/GCE	CA	—	6	40–1000	Urine and serum	65
CZF/CPE	ASV	0.657	2.58×10^{-3}	$0.909–4.70 \times 10^3$	Urine, serum, pharmaceutical preparations	66
SPE	CA	0.031	0.33	13.75–135	DI water	67
TiO_2/PB/AuNPs/CMK-3/Nafion/GE	CV	15.93	1.08×10^{-1}	1–10	Environmental water	68
NP-GCE	DPV	—	0.008	0.25–100	Groundwater and tap water	69
Porous-Nafion-MWCNT/BDD	DPV	41 ± 5.2 and 2.1 ± 0.22	0.005	0.005–0.05, 0.05–10	Natural waters and wastewater effluents.	70
BSA/anti-CPX/APTES/nLa_2O_3/ITO	DPV	11.44 and 7.88	0.000001	0.000001–0.0005 and 0.001–1	Milk	9
BSA/anti-CPX/APTES/nLa_2O_3 NPs@rGO/ITO	**DPV**	**6.52**	**0.005**	**1×10^{-6} – 600**	**Milk**	**This work**

several aspects of the immunosensor's design, including biomolecule binding sites and the immobilization of antibodies (anti-CPX), which may result in different conformation modifications in the structure of the antibody on the electrode. Here, the increased K_a value shows how the constructive anti-CPX conformation as well as greater loading on the electrode's surface have increased the BSA/anti-CPX/APTES/nLa_2O_3 NPs@rGO/ITO immunoelectrode affinity against CPX. The dissociation constant (K_d) was found at -3.2 μg mL^{-1}, indicating a strong, centered CPX affinity. The linear fitting plot of Hanes–Wolf yielded inverse slope values for the K_a calculations, whereas the K_d value is estimated using the intercept and K_a product.[71,72]

Control, interferent, repeatability, and reproducibility studies. A control experiment was conducted to assess the electrochemical current response of the APTES/nLa_2O_3 NPs@rGO/ITO electrode with varying concentrations of CPX, as depicted in Fig. 8(a). All parameters remained consistent with the electrochemical response studies conducted for the BSA/anti-CPX/APTES/nLa_2O_3 NPs@rGO/ITO immunoelectrode, except for the immobilization of monoclonal anti-CPX antibodies. The results indicated no change in DPV current of the APTES/nLa_2O_3 NPs@rGO/ITO electrode when higher concentrations of CPX were introduced. This lack of change in current suggests that there was no interaction occurring between the APTES/nLa_2O_3 NPs@rGO/ITO electrode and CPX, leading to a stable electrochemical response. Therefore, the observed current changes in the response studies primarily stem from the interaction between the CPX antigen and the anti-CPX antibody, rather than the APTES/nLa_2O_3 NPs@rGO/ITO electrode itself.

As we widely understood, foodstuffs are extremely rich in both organic and inorganic analytical substances such as Mg^{++} (0.01 g mL^{-1}), CPX (50 mM), Na^+ (0.6 g100 mL^{-1}), ofloxacin (50 mM), norfloxacin (50 mM), cholesterol (100 M), vitamin C (100 M), glucose (100 M), BSA (100 M), and so forth. The interfering agents were prepared in the milk samples following the respective concentration. Additionally, the sensor response to the CPX was evaluated in milk samples in the presence of different potential interfering agents to test the BSA/anti-CPX/APTES/nLa_2O_3 NPs@rGO/ITO immunosensor's cross-reactivity [Fig. 8(b)]. The constructed BSA/anti-CPX/APTES/nLa_2O_3 NPs@rGO/ITO immunoelectrode was first tested in the presence of a particular CPX concentration. Then, following a 14 min incubation period, a different analyte was gradually added (20 μL at a time) to the electrolyte that had already been premixed by the CPX analyte, and the current output was measured. The current of the whole interferents has been shown to be merely unaltered, demonstrating the biosensor's high specificity for the CPX antigen.

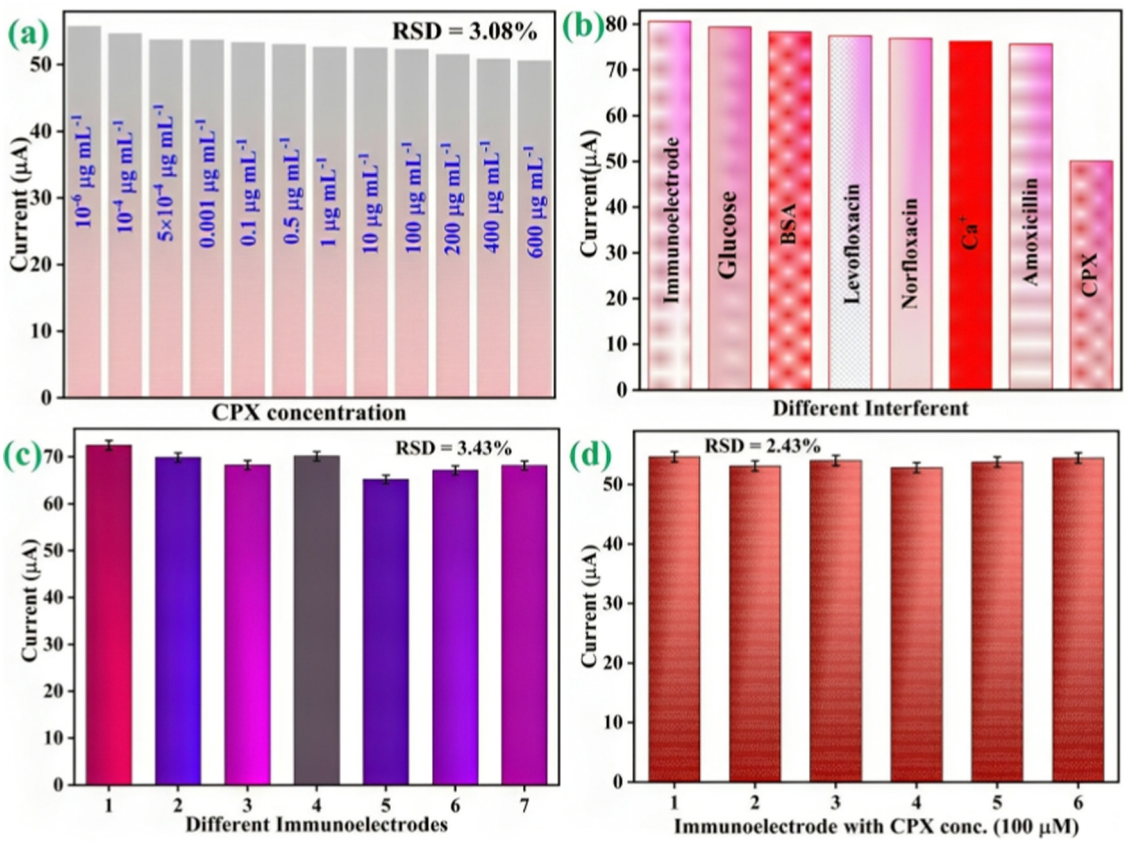

Fig. 8 (a) The APTES/nLa_2O_3 NPs@rGO/ITO electrode showing control studies between the DPV current values *versus* concentration of CPX antigen from 10^{-6}–600 μg mL^{-1}; (b) the BSA/anti-CPX/APTES/nLa_2O_3 NPs@rGO/ITO immunoelectrode depicting the bar graph of different interferents found in the milk sample using the DPV technique; (c) reproducibility; and (d) repeatability responses of the BSA/anti-CPX/APTES/nLa_2O_3 NPs@rGO/ITO immunoelectrode, respectively.

Using eqn (10), the selectivity co-efficient was determined to be 1 for each interfering agent.

$$SC = I_c + I_{c+i} \quad (11)$$

where I_c and I_{c+i} are the immunosensor's current values in absence and presence, respectively, exhibiting barely any change in the response.

By using the DPV approach on seven separate developed electrodes under similar experimental circumstances, the reproducibility of the developed BSA/anti-CPX/APTES/nLa_2O_3 NPs@rGO/ITO immunosensor is examined (data displayed in Fig. 8(c)). Relative standard deviation (% RSD) was determined for every electrode to evaluate the variance of the data from various electrodes to the standard anodic peak current magnitude. The average %RSD was discovered as 3.43%, demonstrating that the calculated % RSD is below an acceptable limit. The BSA/anti-CPX/APTES/nLa_2O_3 NPs@rGO/ITO immunosensor showed good reproducibility as the current response was barely altered. Similar to this, the repeatability of the BSA/anti-CPX/APTES/nLa_2O_3 NPs@rGO/ITO immunosensor was assessed by employing the DPV approach to take six subsequent readings for a specific CPX concentration *i.e.*, 100 μg mL^{-1} [Fig. 8(d)]. The repeatability RSD results have been found as 2.43%, which is within the permitted range.

Regeneration, stability, and spiked sample studies. Regeneration is a crucial characteristic in the creation of affordable biosensors, and the procedure for reusing the fabricated biosensor multiple times. The immunosensor BSA/anti-CPX/APTES/nLa_2O_3 NPs@rGO/ITO was examined following anti-CPX and CPX interactions to assess how well it regenerates. Different kinds of regeneration solutions, including $MgCl_2$ (salt), NaOH (basic), and glycine-HCl buffer or HCl (acidic), were prepared for this study. The CPX–anti-CPX immunological complex was broken in this experiment using 0.010 % Tween-20 and 10 % (1 : 1) formamide/DMSO in PBS (pH 7.0).[52,73] Following that, a specific CPX concentration was once again re-examined using a regenerated immunoelectrode (BSA/anti-CPX/APTES/nLa_2O_3 NPs@rGO/ITO). To evaluate the DPV signal in this investigation, a specific CPX concentration was used [Fig. 9(a)]. Following each regeneration process, the immunosensor electrochemical changes were recorded. The BSA/anti-CPX/APTES/nLa_2O_3 NPs@rGO/ITO immunosensor could potentially be reused for a minimum of four times depicting 95 % retention as well as 5 more times for 84 % retention of the first response that was recorded, as shown in Fig. 9(a).

Furthermore, the BSA/anti-CPX/APTES/nLa_2O_3 NPs@rGO/ITO immunosensor was put to the test using CV at 5 day intervals to determine its stability. The findings displayed in Fig. 9(b) depict that it maintains a current value of 95 % for the

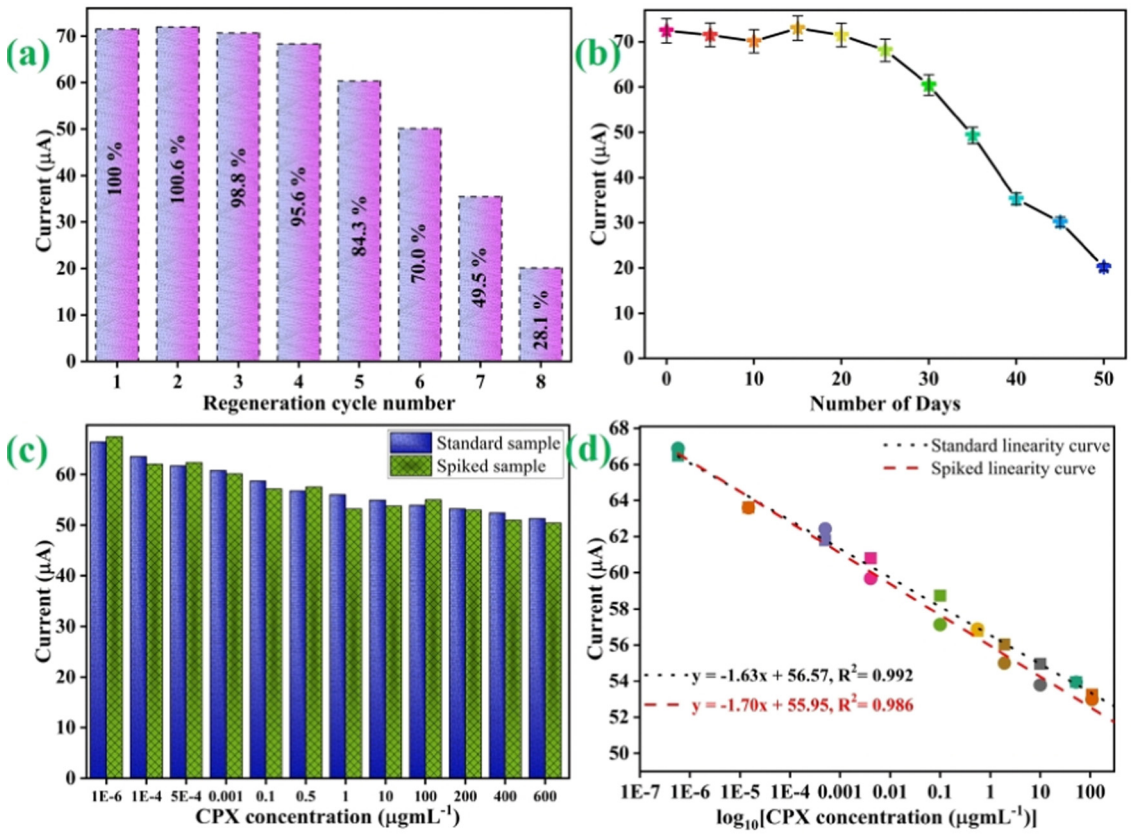

Fig. 9 (a) Regeneration effect studies of the BSA/anti-CPX/APTES/nLa_2O_3 NPs@rGO/ITO immunosensing platform at a particular concentration of CPX; (b) stability of the developed BSA/anti-CPX/APTES/nLa_2O_3 NPs@rGO/ITO immunosensor; (c) real spiked milk sample studies *versus* CPX concentration; and (d) comparative calibration curve in spiked milk and standard samples.

Table 2 The developed BSA/anti-CPX/APTES/nLa_2O_3 NPs@rGO/ITO immunoelectrode showing RSD and recovery of CPX antibiotic in spiked milk samples

Sample	Standard concentrations of CPX ($\mu g\ mL^{-1}$)		RSD (%)	Recovery (%)
	Added concentration	Found concentration		
Milk	0.000001	0.00000107	4.7	107
	0.0001	0.000102	1.4	102
	0.0005	0.00054	5.4	108
	0.001	0.00105	3.4	105
	0.1	0.106	4.1	106
	0.5	0.47	4.3	94
	1	1.12	8.0	112
	10	11.01	6.7	110.1
	100	90.57	6.9	90.57
	200	206.14	2.1	103.07
	400	411.40	1.9	102.85
	600	661.46	6.8	110.24

first 25 days, then slightly declines to 80 % after 35 days. As a result, the manufactured immunosensor has a 25 day durability.

For investigating the exploitation of CPX in a food sample study, the immunosensor's practical use is crucial. To illustrate the ability of the constructed immunosensor to recognize CPX in milk samples, a spiked sample investigation has been examined, as shown in Fig. 9(c). For this, the proposed BSA/anti-CPX/APTES/nLa_2O_3NPs@rGO/ITO immunoelectrode reaction on treated milk was evaluated. However, the milk sample was treated/spiked with particular concentrations of CPX, when no CPX had been identified to evaluate the accuracy of the constructed immunosensor. The diagnostic outcomes for real samples spiked with significant amounts of standard CPX concentration are displayed in Table 2. The immunosensor exhibited outstanding RSD values with recovery rates ranging from 1.4 % to 8.0 % and 90.57 % to 112 %, respectively. These results undeniably showcase the precision and dependability of the developed biosensor in detecting CPX in real-world scenarios.

Additionally, as is apparent from Fig. 9(d), we also examined the linear fitting graph in the presence of spiked milk samples and standard samples. In the standard sample's response, the most suitable linear fitting curve was discovered at 0.992 R^2 value.

4. Conclusion

In conclusion, we have developed an affordable, highly sensitive, efficient, and simple nLa_2O_3 NPs@rGO/ITO nano-immunosensor to identify CPX. We introduced the first label-free immunosensor for the determination of CPX comprising a nLa_2O_3 NPs@rGO nanocomposite. The fascinating features of rGO and nLa_2O_3 work together synergistically to improve the electrochemical properties. Additionally, the rGO addition enhanced the sensitivity of the immunosensor by creating –COOH adsorption locations for CPX and reducing the nLa_2O_3 NP aggregation through its large surface area. The application of the nanocomposite contributes to the achievement of a broad linear range determination *i.e.*, 1×10^{-6} to 600 $\mu g\ mL^{-1}$ covering both released and deadly concentrations of CPX having a 0.992 regression coefficient (R^2) as well as a lower LOD of 0.055 $\mu g\ mL^{-1}$with a greater sensitivity of 6.52 $\mu A\ mL\ \mu g^{-1}\ cm^2$. Additionally, the designed nano-immunosensor has a 25 day high durability. The nLa_2O_3 NPs@rGO composite offers tremendous potential for biomedical uses as well as for the development of nano-immunosensors for other food contaminant determination. More effort should be undertaken to examine how well the constructed nano-immunosensor performs with real food samples.

Author contributions

Navneet Chaudhary: formal analysis, investigation, writing – original draft. Amit K. Yadav: conceptualization, methodology, formal analysis, investigation, writing – original draft, writing – review & editing. Damini Verma: writing-original draft, writing – review & editing, Prof Jai Gopal Sharma: supervision, validation, writing – review &editing; Pratima R Solanki: conceptualization, methodology, supervision, validation, writing – review &editing.

Conflicts of interest

There are no conflicts of interest to declare.

Acknowledgements

The Advanced Instrumentation Research Facilities (AIRF), JNU provided the essential characterization amenities, which the authors gratefully acknowledge. The Indian Council of Medical Research (ICMR) sponsored project No. 34/13/2019-TF/Nano/BMS, New Delhi, India; the Department of Biotechnology (DBT) sponsored Indo-Russia Project (DBT/IC-2/Indo-Russia/2017-19/02); and the Department of Science and Technology (DST) sponsored project No. TDP/BDTD/49/2021 are all acknowledged with appreciation for their financial support. For the ICMR-SRF fellowship, Navneet Chaudhary expresses gratitude to the ICMR in India. Amit K. Yadav extends admiration to the Ministry of Education, Government of India, for the financial support provided by the Prime Minister Research Fellowship (PMRF).

References

1 V. F. Samanidou, C. E. Demetriou and I. N. Papadoyannis, Direct determination of four fluoroquinolones, enoxacin, norfloxacin, ofloxacin, and ciprofloxacin, in pharmaceuticals and blood serum by HPLC, *Anal. Bioanal. Chem.*, 2003, **375**, 623–629.
2 J. Bertino Jr and D. Fish, The safety profile of the fluoroquinolones, *Clin. Ther.*, 2000, **22**(7), 798–817.
3 C. Fierens, S. Hillaert and W. Van den Bossche, The qualitative and quantitative determination of quinolones of first and second generation by capillary electrophoresis, *J. Pharm. Biomed. Anal.*, 2000, **22**(5), 763–772.

4 C. B. Inderlied and K. A. Nash, *Antibiotics in laboratory medicine*, Lippincott Williams & Wilkins, Philadelphia, 1996, pp. 127–129.
5 A. H. Gilani, S. Bashir, K. H. Janbaz and A. Khan, Pharmacological basis for the use of Fumaria indica in constipation and diarrhea, *J. Ethnopharmacol.*, 2005, **96**(3), 585–589.
6 D. G. J. Larsson, C. de Pedro and N. Paxeus, Effluent from drug manufactures contains extremely high levels of pharmaceuticals, *J. Hazard. Mater.*, 2007, **148**(3), 751–755.
7 S. Pakpinyo and J. Sasipreeyajan, Molecular characterization and determination of antimicrobial resistance of Mycoplasma gallisepticum isolated from chickens, *Vet. Microbiol.*, 2007, **125**(1–2), 59–65.
8 S. C. Chang, Y. C. Chen, K. T. Luh and W. C. Hsieh, In vitro activites of antimicrobial agents, alone and in combination, against Acinetobacter baumannii isolated from blood, *Diagn. Microbiol. Infect. Dis.*, 1995, **23**(3), 105–110.
9 N. Chaudhary, A. K. Yadav, J. G. Sharma and P. R. Solanki, Designing and characterization of a highly sensitive and selective biosensing platform for ciprofloxacin detection utilizing lanthanum oxide nanoparticles, *J. Environ. Chem. Eng.*, 2021, **9**(6), 106771.
10 A. Radi, M. A. El Ries and S. Kandil, Electrochemical study of the interaction of levofloxacin with DNA, *Anal. Chim. Acta*, 2003, **495**(1–2), 61–67.
11 G. G. Snitkoff, D. W. Grabe, R. Holt and G. R. Bailie, Development of an Immunoassay for Monitoring the Levels of Ciprofloxacin Patient Samples, *J. Immunoassay Immunochem.*, 1998, **19**(4), 227–238.
12 S. Mostafa, M. El-Sadek and E. A. Alla, Spectrophotometric determination of ciprofloxacin, enrofloxacin and pefloxacin through charge transfer complex formation, *J. Pharm. Biomed. Anal.*, 2002, **27**(1–2), 133–142.
13 R. H. O. Montes, M. C. Marra, M. M. Rodrigues, E. M. Richter and R. A. A. Muñoz, Fast determination of ciprofloxacin by batch injection analysis with amperometric detection and capillary electrophoresis with capacitively coupled contactless conductivity detection, *Electroanalysis*, 2014, **26**(2), 432–438.
14 H. W. Sun, L. Q. Li and X. Y. Chen, Flow-injection enhanced chemiluminescence method for determination of ciprofloxacin in pharmaceutical preparations and biological fluids, *Anal. Bioanal. Chem.*, 2006, **384**, 1314–1319.
15 Y. Ni, Y. Wang and S. Kokot, Multicomponent kinetic spectrophotometric determination of pefloxacin and norfloxacin in pharmaceutical preparations and human plasma samples with the aid of chemometrics, *Spectrochim. Acta, Part A*, 2008, **70**(5), 1049–1059.
16 Y. Liang, C. Yu and J. Song, Cathodic electrochemiluminescence of the peroxydisulphate–ciprofloxacin system and its analytical applications, *Luminescence*, 2011, **26**(6), 662–669.
17 G. H. Wan, H. Cui, Y. L. Pan, P. Zheng and L. J. Liu, Determination of quinolones residues in prawn using high-performance liquid chromatography with Ce (IV)–Ru (bpy) 32 + –HNO_3 chemiluminescence detection, *J. Chromatogr. B: Anal. Technol. Biomed. Life Sci.*, 2006, **843**(1), 1–9.
18 H. Y. Ji, D. W. Jeong, Y. H. Kim, H.-H. Kim, D.-R. Sohn and H. S. Lee, Hydrophilic interaction liquid chromatography–tandem mass spectrometry for the determination of levofloxacin in human plasma, *J. Pharm. Biomed. Anal.*, 2006, **41**(2), 622–627.
19 A. K. Yadav, D. Verma and P. R. Solanki, Electrophoretically deposited L-cysteine functionalized MoS_2@MWCNT nanocomposite platform: a smart approach toward highly sensitive and label-free detection of gentamicin, *Mater. Today Chem.*, 2021, **22**, 100567, DOI: **10.1016/J.MTCHEM.2021.100567**.
20 A. K. Yadav, T. K. Dhiman, G. Lakshmi, A. N. Berlina and P. R. Solanki, A highly sensitive label-free amperometric biosensor for norfloxacin detection based on chitosan-yttria nanocomposite, *Int. J. Biol. Macromol.*, 2020, **151**, 566–575.
21 J. M. Moon, D. M. Kim, M. H. Kim, J. Y. Han, D. K. Jung and Y. B. Shim, A disposable amperometric dual-sensor for the detection of hemoglobin and glycated hemoglobin in a finger prick blood sample, *Biosens. Bioelectron.*, 2017, **91**, 128–135.
22 S. Chung, J. M. Moon, J. Choi, H. Hwang and Y. B. Shim, Magnetic force assisted electrochemical sensor for the detection of thrombin with aptamer-antibody sandwich formation, *Biosens. Bioelectron.*, 2018, **117**, 480–486.
23 A. C. Sun and D. A. Hall, Point-of-care smartphone-based electrochemical biosensing, *Electroanalysis*, 2019, **31**(1), 2–16.
24 S. Bhattacharya, R. Maiti, M. B. Sen, S. K. Saha and D. Chakravorty, Anomalous enhancement in the magnetoconductance of graphene/$CoFe_2O_4$ composite due to spin–orbit coupling, *J. Phys. D: Appl. Phys.*, 2015, **48**(43), 435002.
25 P. Hota, A. J. Akhtar, S. Bhattacharya, M. Miah and S. K. Saha, Ferromagnetism in graphene due to charge transfer from atomic Co to graphene, *Appl. Phys. Lett.*, 2017, **111**(4), 42402.
26 X. Zhu, *et al.*, Syntheses, structures and photoluminescence of a series of lanthanide-organic frameworks involving in situ ligand formation, *J. Solid State Chem.*, 2009, **182**(3), 421–427.
27 D. Lin, *et al.*, High ionic conductivity of composite solid polymer electrolyte via in situ synthesis of monodispersed SiO_2 nanospheres in poly (ethylene oxide), *Nano Lett.*, 2016, **16**(1), 459–465.
28 Z. Li, X. Hou, L. Yu, Z. Zhang and P. Zhang, Preparation of lanthanum trifluoride nanoparticles surface-capped by tributyl phosphate and evaluation of their tribological properties as lubricant additive in liquid paraffin, *Appl. Surf. Sci.*, 2014, **292**, 971–977.
29 C. Tan, X. Huang and H. Zhang, Synthesis and applications of graphene-based noble metal nanostructures, *Mater. Today*, 2013, **16**(1–2), 29–36.
30 R. Kumar, R. K. Singh, P. K. Dubey, D. P. Singh and R. M. Yadav, Self-assembled hierarchical formation of conjugated 3D cobalt oxide nanobead–CNT–graphene nanostructure using microwaves for high-performance supercapacitor electrode, *ACS Appl. Mater. Interfaces*, 2015, **7**(27), 15042–15051.
31 R. Kumar, M. M. Abdel-Galeil, K. Z. Ya, K. Fujita, W. K. Tan and A. Matsuda, Facile and fast microwave-assisted

formation of reduced graphene oxide-wrapped manganese cobaltite ternary hybrids as improved supercapacitor electrode material, *Appl. Surf. Sci.*, 2019, **481**, 296–306.

32 R. Kumar, E. Joanni, R. K. Singh, D. P. Singh and S. A. Moshkalev, Recent advances in the synthesis and modification of carbon-based 2D materials for application in energy conversion and storage, *Prog. Energy Combust. Sci.*, 2018, **67**, 115–157.

33 I. S. El-Hallag, M. N. El-Nahass, S. M. Youssry, R. Kumar, M. M. Abdel-Galeil and A. Matsuda, Facile in-situ simultaneous electrochemical reduction and deposition of reduced graphene oxide embedded palladium nanoparticles as high performance electrode materials for supercapacitor with excellent rate capability, *Electrochim. Acta*, 2019, **314**, 124–134.

34 R. Kumar, R. K. Singh, D. P. Singh, E. Joanni, R. M. Yadav and S. A. Moshkalev, Laser-assisted synthesis, reduction and micro-patterning of graphene: Recent progress and applications, *Coord. Chem. Rev.*, 2017, **342**, 34–79.

35 A. Devadoss, *et al.*, Ultrathin functional polymer modified graphene for enhanced enzymatic electrochemical sensing, *Biosensors*, 2019, **9**(1), 16.

36 N. G. Hallfors, S. A. Al Junaibi, K. Liao, M. Ismail and A. F. Isakovic, Reduced Graphene oxide for the design of electrocardiogram sensors: Current status and perspectives, *IoT Phys. Layer Des. Implement.*, 2019, 3–11.

37 P. K. Gupta, Z. H. Khan and P. R. Solanki, Improved electrochemical performance of metal doped Zirconia nanoparticles for detection of Ochratoxin-A, *J. Electroanal. Chem.*, 2018, **829**, 69–80.

38 S. Kumar, J. G. Sharma, S. Maji and B. D. Malhotra, Nanostructured zirconia decorated reduced graphene oxide based efficient biosensing platform for non-invasive oral cancer detection, *Biosens. Bioelectron.*, 2016, **78**, 497–504.

39 Y. Li, *et al.*, Nitidine chloride-assisted bio-functionalization of reduced graphene oxide by bovine serum albumin for impedimetric immunosensing, *Biosens. Bioelectron.*, 2016, **79**, 536–542.

40 Y. Chen, *et al.*, Effective immobilization of Au nanoparticles on TiO_2 loaded graphene for a novel sandwich-type immunosensor, *Biosens. Bioelectron.*, 2018, **102**, 301–306.

41 D. Verma, A. K. Yadav, M. Das Mukherjee and P. R. Solanki, Fabrication of a sensitive electrochemical sensor platform using reduced graphene oxide-molybdenum trioxide nanocomposite for BPA detection: An endocrine disruptor, *J. Environ. Chem. Eng.*, 2021, **9**(4), 105504.

42 A. K. Yadav, D. Verma and P. R. Solanki, Enhanced Electrochemical Biosensing of the Sp17 Cancer Biomarker in Serum Samples via Engineered Two-Dimensional MoS_2 Nanosheets on the Reduced Graphene Oxide Interface, *ACS Appl. Bio Mater.*, 2023, **6**(10), 4250–4268.

43 A. K. Yadav, P. Gulati, R. Sharma, A. Thakkar and P. R. Solanki, Fabrication of alkoxysilane substituted polymer-modified disposable biosensing platform: Toward sperm protein 17 sensing as a new cancer biomarker, *Talanta*, 2022, 123376.

44 A. K. Yadav, D. Verma, G. Lakshmi, S. Eremin and P. R. Solanki, Fabrication of label-free and ultrasensitive electrochemical immunosensor based on molybdenum disulfide nanoparticles modified disposable ITO: An analytical platform for antibiotic detection in food samples, *Food Chem.*, 2021, **363**, 130245.

45 R. Rajagopal, A. Ragunathan, S. M. Senthil Kumar, R. Krishnan and B. A. Kamaludeen, Synthesis and electrochemical studies of Ta–Graphene nanocomposite film modified platinum electrode, *J. Electroanal. Chem.*, 2016, **780**, 53–59.

46 P. Cui, J. Lee, E. Hwang and H. Lee, One-pot reduction of graphene oxide at subzero temperatures, *Chem. Commun.*, 2011, **47**(45), 12370–12372.

47 R. Senthil Kumar and B. Gnanavel, High performance catalytic activity of pure and silver (Ag) doped TiO_2 nanoparticles by a novel microwave irradiation technique, *J. Mater. Sci.: Mater. Electron.*, 2017, **28**, 4253–4259.

48 M. Salavati-Niasari, G. Hosseinzadeh and F. Davar, Synthesis of lanthanum carbonate nanoparticles *via* sonochemical method for preparation of lanthanum hydroxide and lanthanum oxide nanoparticles, *J. Alloys Compd.*, 2011, **509**(1), 134–140.

49 R. B. Borade, *et al.*, Polycrystalline to preferred-(100) single crystal texture phase transformation of yttrium iron garnet nanoparticles, *Nanoscale Adv.*, 2019, **1**(1), 403–413.

50 Q. Zhou, *et al.*, Nano La_2O_3 as a heterogeneous catalyst for biodiesel synthesis by transesterification of Jatropha curcas L. oil, *J. Ind. Eng. Chem.*, 2015, **31**, 385–392.

51 S. Augustine, P. Kumar and B. D. Malhotra, Amine-functionalized MoO_3@ RGO nanohybrid-based biosensor for breast cancer detection, *ACS Appl. Bio Mater.*, 2019, **2**(12), 5366–5378.

52 A. K. Yadav, D. Verma, A. Kumar, A. N. Bhatt and P. R. Solanki, Biocompatible epoxysilane substituted polymer-based nano biosensing platform for label-free detection of cancer biomarker SP17 in patient serum samples, *Int. J. Biol. Macromol.*, 2023, 124325.

53 S. Kumar, Y. Lei, N. H. Alshareef, M. A. Quevedo-Lopez and K. N. Salama, Biofunctionalized two-dimensional Ti_3C_2 MXenes for ultrasensitive detection of cancer biomarker, *Biosens. Bioelectron.*, 2018, **121**, 243–249.

54 M. Zhou, Y. Zhai and S. Dong, Electrochemical sensing and biosensing platform based on chemically reduced graphene oxide, *Anal. Chem.*, 2009, **81**(14), 5603–5613.

55 S. Kumar, *et al.*, Biofunctionalized nanostructured zirconia for biomedical application: a smart approach for oral cancer detection, *Adv. Sci.*, 2015, **2**(8), 1500048.

56 S. Tiwari, P. K. Gupta, Y. Bagbi, T. Sarkar and P. R. Solanki, L-cysteine capped lanthanum hydroxide nanostructures for non-invasive detection of oral cancer biomarker, *Biosens. Bioelectron.*, 2017, **89**, 1042–1052.

57 D. Verma, D. Chauhan, M. Das Mukherjee, K. R. Ranjan, A. K. Yadav and P. R. Solanki, Development of MWCNT decorated with green synthesized AgNps-based electrochemical sensor for highly sensitive detection of BPA, *J. Appl. Electrochem.*, 2021, **51**(3), 447–462.

58 S. Kumar, *et al.*, Highly sensitive protein functionalized nanostructured hafnium oxide based biosensing platform

for non-invasive oral cancer detection, *Sens. Actuators, B*, 2016, **235**, 1–10.

59 P. K. Gupta, Z. H. Khan and P. R. Solanki, One-step electrodeposited porous ZnO thin film based immunosensor for detection of Vibrio cholerae toxin, *J. Electrochem. Soc.*, 2016, **163**(7), B309.

60 A. A. Ensafi, A. R. Allafchian and R. Mohammadzadeh, Characterization of $MgFe_2O_4$ nanoparticles as a novel electrochemical sensor: application for the voltammetric determination of ciprofloxacin, *Anal. Sci.*, 2012, **28**(7), 705–710.

61 X. Zhang, Y. Wei and Y. Ding, Electrocatalytic oxidation and voltammetric determination of ciprofloxacin employing poly (alizarin red)/graphene composite film in the presence of ascorbic acid, uric acid and dopamine, *Anal. Chim. Acta*, 2014, **835**, 29–36.

62 F. Zhang, S. Gu, Y. Ding, Z. Zhang and L. Li, A novel sensor based on electropolymerization of β-cyclodextrin and l-arginine on carbon paste electrode for determination of fluoroquinolones, *Anal. Chim. Acta*, 2013, **770**, 53–61.

63 H. Nawaz, S. Rauf, K. Akhtar and A. M. Khalid, Electrochemical DNA biosensor for the study of ciprofloxacin–DNA interaction, *Anal. Biochem.*, 2006, **354**(1), 28–34.

64 A. M. Santos, A. Wong, A. A. Almeida and O. Fatibello-Filho, Simultaneous determination of paracetamol and ciprofloxacin in biological fluid samples using a glassy carbon electrode modified with graphene oxide and nickel oxide nanoparticles, *Talanta*, 2017, **174**, 610–618.

65 L. Fotouhi and M. Alahyari, Electrochemical behavior and analytical application of ciprofloxacin using a multi-walled nanotube composite film-glassy carbon electrode, *Colloids Surf., B*, 2010, **81**(1), 110–114.

66 M. P. Kingsley, P. K. Kalambate and A. K. Srivastava, Simultaneous determination of ciprofloxacin and paracetamol by adsorptive stripping voltammetry using copper zinc ferrite nanoparticles modified carbon paste electrode, *RSC Adv.*, 2016, **6**(18), 15101–15111.

67 D. Ganta, N. Trevino and W. Montes, Disposable chronoamperometric sensor for detecting ciprofloxacin, *Eng. Res. Express*, 2019, **1**(1), 15031.

68 A. Pollap and J. Kochana, Electrochemical immunosensors for antibiotic detection, *Biosensors*, 2019, **9**(2), 61.

69 T. Chen, *et al.*, Highly efficient detection of ciprofloxacin in water using a nitrogen-doped carbon electrode fabricated through plasma modification, *New J. Chem.*, 2019, **43**(38), 15169–15176.

70 P. Gayen and B. P. Chaplin, Selective electrochemical detection of ciprofloxacin with a porous Nafion/multiwalled carbon nanotube composite film electrode, *ACS Appl. Mater. Interfaces*, 2016, **8**(3), 1615–1626.

71 D. Chauhan, A. K. Yadav and P. R. Solanki, Carbon cloth-based immunosensor for detection of 25-hydroxy vitamin D 3, *Microchim. Acta*, 2021, **188**(4), 1–11.

72 A. K. Yadav, P. Gulati, R. Sharma, A. Thakkar and P. R. Solanki, Fabrication of alkoxysilane substituted polymer-modified disposable biosensing platform: Towards sperm protein 17 sensing as a new cancer biomarker, *Talanta*, 2022, **243**, 123376.

73 A. Sangili, T. Kalyani, S.-M. Chen, A. Nanda and S. K. Jana, Label-free electrochemical immunosensor based on one-step electrochemical deposition of AuNP-RGO nanocomposites for detection of endometriosis marker CA 125, *ACS Appl. Bio Mater.*, 2020, **3**(11), 7620–7630.